High responsivity all-fiber-integrated perovskite photodetector based on FA0.4MA0.6PbI3

YuChen Zhang

2387775430@qq.com

Tianjin University of Technology https://orcid.org/0009-0003-1221-7901

Jie Liu

Tianjin University of Technology

Chenghong Ma

Tianjin University of Technology

Yanqi Fan

Tianjin University of Technology

Yinping Miao

Hong Kong Polytechnic University

Xiaolan Li

Tianjin University of Technology

Article

Keywords: all-fiber-integrated, perovskite photodetector, side-polished fiber, high responsivity, active layer thickness design

Posted Date: March 20th, 2024

DOI: https://doi.org/10.21203/rs.3.rs-4105126/v1

Additional Declarations: There is **NO** Competing Interest.

High responsivity all-fiber-integrated perovskite photodetector based on $FA_{0.4}MA_{0.6}PbI_3$

Yuchen Zhang[1], Jie Liu[2], Chenghong Ma[2], Yanqi Fan[2], Yinping Miao[1,*] and Xiaolan Li[1,*].

[1]*Tianjin Key Laboratory of Film Electronic and Communication Device, School of Integrated Circuit Science and Engineering, Tianjin University of Technology, Tianjin 300384, China.*

[2]*Key Laboratory of Quantum Optics and Intelligent Photonics, School of Science, Tianjin University of Technology, Tianjin 300384, China.*

**Corresponding author E-mail addresses:*

kikosi@126.com (Yinping Miao); lxl6788@163.com (Xiaolan Li).

Abstract: Perovskite exhibits advantages including tunable bandgap, high absorbance and self-assembly, making it potential for high-performance photodetection. In this study, we report an all-fiber-integrated photodetector (AFPD) based on $FA_{0.4}MA_{0.6}PbI_3$ perovskite. The thickness of photodetector's active layer is designed based on the thin-film waveguide mechanism to optimize device's responsivity. Theoretical analysis and simulation results indicate the presence of a strong mode field in the active layer meeting the resonance thickness condition, which exhibits the potential to enhance material's light absorption efficiency and improve device's responsivity even in a thinned film. Metal-Semiconductor-Metal (MSM) photodetector based on $FA_{0.4}MA_{0.6}PbI_3$ is directly deposited onto a side-polished multimode fiber (SP-MMF). Light transmitted in fiber leaks from core to the MSM photodetector through the polished surface of SP-MMF, inducing a detection response. Experimental results demonstrate that the device achieves a responsivity of 3.2 A/W to 650 nm light, with both rising and falling edges of the response time reaching 8ms. The proposed AFPD exhibits advantages including high responsivity, short response time, low insertion loss and all-fiber integration, providing a reliable solution for the development of high performance AFPD.

Key words:

all-fiber-integrated, perovskite photodetector, side-polished fiber, high responsivity, active layer thickness design

1. Introduction

The perovskite materials exhibit several advantages including tunable bandgaps, high light absorption rates, long carrier diffusion distances, and self-assembly, rendering them with extensive application potential in the field of photodetection[1, 2]. However, existing perovskite photodetectors face a trade-off between responsivity and response time in terms of principles and device structure[3], and their performance still required to be further improved[4].

The waveguide-coupled AFPD is a low-loss photodetector based on evanescent field coupling[5]. As the photodetector is part of the waveguide, it not only exhibits the advantage of low insertion loss but also extends the effective absorption distance of the active layer, showing a "long-range effect" that enhances device's responsivity[6]. Therefore, the waveguide-coupled AFPD is potential to simultaneously achieve high responsivity and fast response. Various fiber-integrated photodetectors employing different fiber structures including nanofiber[7], photonic crystal fiber[8], and side-polished fiber[6, 9, 10] have been reported, showcasing improvement in responsivity and response time. Among

these, side-polished fiber stands out due to its a large flat operating surface area and evanescent field, rendering it an ideal platform for AFPD. However, further exploration is needed to find the performance enhancement mechanisms and approaches for perovskite-based AFPD that achieve high responsivity and short response time simultaneously.

The dual cation perovskite $FA_{0.4}MA_{0.6}PbI_3$ has been demonstrated to have advantages including high absorbance, good stability, and fewer surface defects in previous studies[11]. The bandgap and absorption edge of $FA_{0.4}MA_{0.6}PbI_3$ are reported as 1.55 eV and 800 nm, respectively[12]. This proximity to the low-loss transmission window of multimode fibers (MMF) indicates its potential for achieving high-performance AFPD. The MSM photodetector can be composed solely of $FA_{0.4}MA_{0.6}PbI_3$ thin film and interdigitated electrodes, providing the advantage of a straightforward device structure. This configuration facilitates the direct deposition of the active layer onto the polished surface of SP-MMF, demonstrating promising potential for efficient evanescent field coupling. Therefore, the MSM photodetector is an ideal device form for AFPD.

In this study, we present a waveguide-coupled AFPD based on $FA_{0.4}MA_{0.6}PbI_3$, and designed the thickness of photodetector's active layer based on the thin-film waveguide mechanism to optimize its performance. Theoretical analysis and simulation results demonstrate the presence of a strong mode field in the active layer that satisfies the resonance thickness condition, indicating the potential for improving the device's absorptivity and responsivity. The $FA_{0.4}MA_{0.6}PbI_3$ MSM photodetector is directly integrated onto the polished surface of SP-MMF, where the transmitted light in fiber core leaks to the photodetector, inducing photoelectric response. Experimental results indicating that the proposed AFPD achieves a responsivity of 3.2 A/W for 650 nm light with a response time of 8 ms for both rise and fall edge. The proposed AFPD exhibits advantages of high responsivity, short response time, low insertion loss and all-fiber integration, making it a promising design for the development of high-performance AFPD.

2. Methods

2.1 schematic diagram of AFPD

The structure of the proposed AFPD is illustrated in Fig. 1. The MSM photodetector based on $FA_{0.4}MA_{0.6}PbI_3$ is directly integrated onto a SP-MMF. Light transmitted in fiber core leaks to the active layer of the MSM photodetector through the polished surface, inducing a detection response.

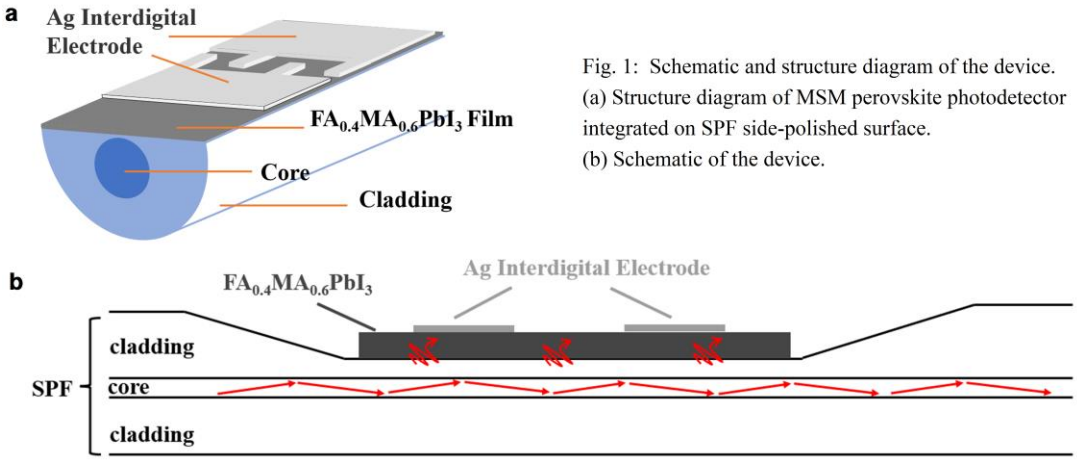

Fig. 1: Schematic and structure diagram of the device. (a) Structure diagram of MSM perovskite photodetector integrated on SPF side-polished surface. (b) Schematic of the device.

2.2 thickness design of AFPD's active layer

The active layer of AFPD can be considered as a thin-film waveguide, and the proposed photodetector can be simplified to the structure shown in Fig. 2(a). The core diameter and refractive index of SP-MMF are 62.5μm and 1.472. The cladding diameter is 125μm with a refractive index of 1.4565. The remaining cladding thickness after polishing is defined as 500 nm, and the thickness of the perovskite film is set to 564 nm with a refractive index of 2.188[11]. The wavelength used for simulation is 650 nm. As shown in Fig. 2(b), the simulation results demonstrate resonance occurring in the perovskite thin film layer, where constructive interference leads to the formation of strong mode fields. In the coordinate system depicted in Fig. 2(a), with the origin point O as the reference, the variation of the electric field intensity of the fundamental mode along the positive y-axis direction of Fig. 2(b) is shown in Fig. 2(c). The simulation results indicate the presence of a strong mode field in the active layer of a specific thickness, which is potential for enhancing the coupling efficiency between light and active layer of photodetector, thereby improving device's responsivity.

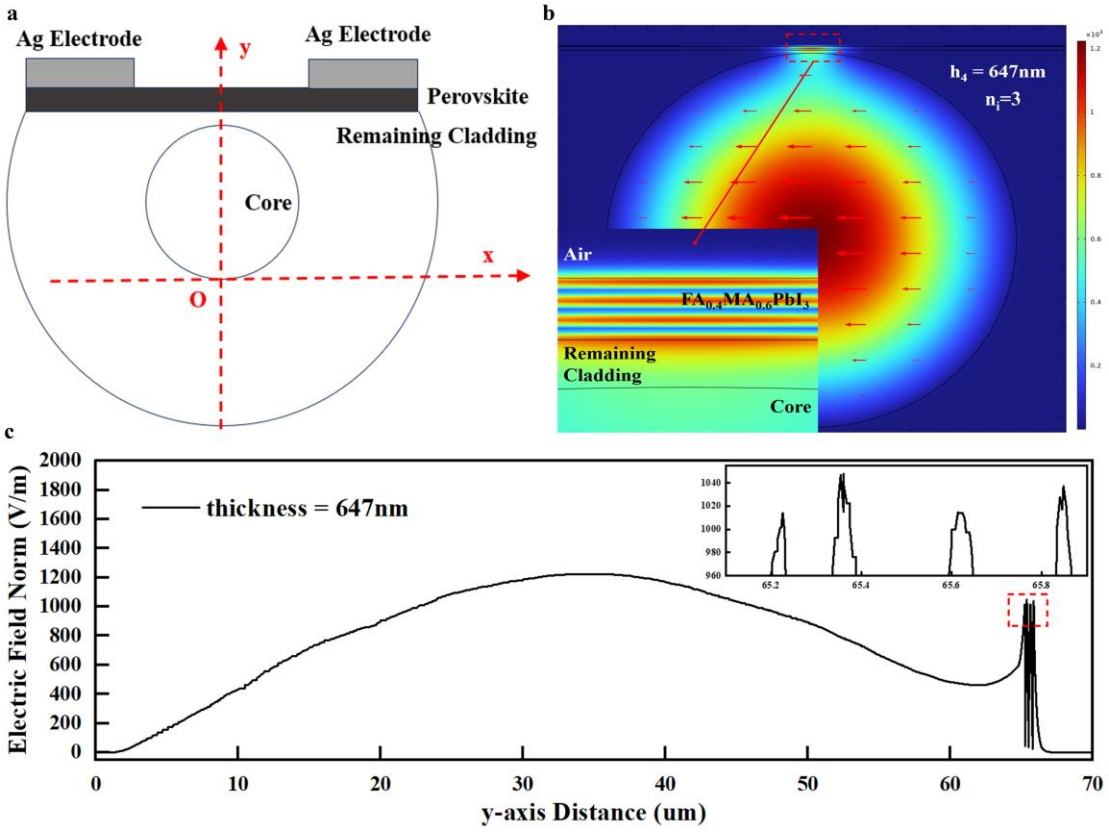

Fig. 2: Mode field in 564 nm thick $FA_{0.4}MA_{0.6}PbI_3$ thin film. (a) Simplified schematic of the device. (b) Mode field distribution obtained from simulations for the $FA_{0.4}MA_{0.6}PbI_3$ film with a thickness of 564 nm. (c) Variation of electric field intensity along the positive y-axis in the simplified schematic diagram.

Since the mode field in the perovskite thin film shown in Fig. 2(b) distributes near and along the y-axis in Fig. 2(a), the model depicted in Fig. 2(a) can be simplified to the five-layer slab waveguide structure shown in Fig. 3(a). Theoretical analysis and explanations for the resonance thickness conditions of the perovskite film were explored based on this model. The refractive index of air is denoted as n_3. The refractive index of $FA_{0.4}MA_{0.6}PbI_3$ is denoted as n_4, with a thickness denoted as h_4. The refractive index of remaining cladding of the polished area is denoted as n_2, with a thickness denoted as h_2. The

refractive index of core is denoted as n_1, with a thickness denoted as h_1.The refractive indices for air, perovskite, remaining cladding, and fiber core are considered as certain values: n_3 = 1, n_4 = 2.188, n_2 = 1.4565, n_1 = 1.472. The diameter of core is 62.5 nm, and the thickness of remaining cladding of the polished area is defined as h_2 = 500 nm.

For the model in Fig. 3(a), a strong TE mode is expected to exist in the $FA_{0.4}MA_{0.6}PbI_3$ layer by designing the value of h_4, aiming to enhance the material's light absorption and device's responsivity. TE modes in the thin film can only exist in either oscillatory or decay forms. Thus, TE modes must be distributed in oscillatory form as a strong mode field is desired in the $FA_{0.4}MA_{0.6}PbI_3$ layer. Therefore, the following condition needed to be satisfied:

$$n_4 k_0 > \beta > n_2 k_0 \quad \textbf{(1)}$$

Mode effective refractive index needs to conform to:

$$n_4 > N > n_2 \quad \textbf{(2)}$$

Where N represents the mode effective refractive index, k_0 is the wave number, and β is the propagation constant.

The guided mode of the $FA_{0.4}MA_{0.6}PbI_3$ layer is physically excited by the evanescent field of core, the field equation of E_x component in the remaining cladding layer conforms to decay form with $y = h_1$ as the beginning. The field equations of E_x component for each layer can be described as following:

$$E_x = \begin{cases} A_3 e^{-p_3(y-h_1-h_2-h_4)} & y > h_1+h_2+h_4 \quad \textbf{(3)} \\ A_4 \cos(\kappa_4 y + \varphi_4) & h_1+h_2 < y < h_1+h_2+h_4 \quad \textbf{(4)} \\ A_2 e^{-p_2(y-h_1)} & h_1 < y < h_1+h_2 \quad \textbf{(5)} \\ A_1 \cos(\kappa_1 y + \varphi_1) & 0 < y < h_1 \quad \textbf{(6)} \\ A_5 e^{p_2 y} & y < 0 \quad \textbf{(7)} \end{cases}$$

The details of p_3 , κ_4 , p_2 , and κ_1 can be found in the supplementary document. According to equation (4), the intensity of guided mode of $FA_{0.4}MA_{0.6}PbI_3$ layer primarily depends on the constant coefficient A_4. Based on the boundary continuity conditions, E_x and $\frac{E_x}{dy}$ are continuous at the boundary $y = h_1 + h_2$. The value of A_4 follows the following two equations:

$$A_4 \cos[\kappa_4(h_1+h_2)+\varphi_4] = A_2 e^{-p_2 h_2} \quad \textbf{(8)}$$

$$A_4 \kappa_4 \sin[\kappa_4(h_1+h_2)+\varphi_4] = A_2 e^{-p_2 h_2} \quad \textbf{(9)}$$

Equations (8) and (9) can be squared and summed to yield:

$$A_4 = A_2 \sqrt{1+\frac{p_2^2}{\kappa_4^2}}\, e^{-p_2 h_2} \quad \textbf{(10)}$$

Performing the same process for A_2, equation (11) can be obtained:

$$A_4 = A_1 \sqrt{\left(1-\frac{n_4^2-n_1^2}{n_4^2-N^2}\right)\left(1+\frac{n_4^2-n_1^2}{n_1^2-n_2^2}\right)}\, e^{-p_2 h_2} \quad \textbf{(11)}$$

From Equation (11), the intensity of guided mode of the $FA_{0.4}MA_{0.6}PbI_3$ layer depends on N, and the intensity of the TE mode in the film increases as N decreases. Analysis results indicates that by controlling the effective refractive index N, the intensity of the mode field in the $FA_{0.4}MA_{0.6}PbI_3$ layer can be enhanced.

According to the boundary continuity conditions, at $y = h_1 + h_2 + h_4$, equation (12) can be obtained:

$$\arctan\frac{p_3}{\kappa_4} = \kappa_4(h_1+h_2+h_4)+\varphi_4+m_1\pi \quad \textbf{(12)}$$

at $y = h_1 + h_2$, equation (13) can be obtained:

$$\arctan\frac{p_2}{\kappa_4} = \kappa_4(h_1+h_2)+\varphi_4+m_2\pi \quad \textbf{(13)}$$

Subtracting Equation (12) from Equation (13) and substituting p_3, κ_4, p_2 into the result, the transcendental equation between the film thickness h_4 and the effective refractive index N can be obtained:

$$arctan\frac{\sqrt{N^2-n_3^2}}{\sqrt{n_4^2-N^2}} - arctan\frac{\sqrt{N^2-n_2^2}}{\sqrt{n_4^2-N^2}} = k_0\sqrt{n_4^2-N^2}h_4 + n_i\pi \quad \textbf{(14)}$$

In equation (14), $n_i\pi$ represents the resonance order in the $FA_{0.4}MA_{0.6}PbI_3$ film, where $n_i = 0, 1, 2, 3\cdots$. The curve illustrating the relationship between the effective refractive index N and the thickness h_4 of the $FA_{0.4}MA_{0.6}PbI_3$ film , as calculated from Equation (14), is depicted in Fig. 3(b). The flat section in Fig. 3(b) denotes the non-resonant range of h_4, where the corresponding effective refractive index N fails to satisfy Equation (2), and TE mode in the film does not meet the criteria for oscillation. According to Equation (11), as N decreases, the resonance intensity of TE modes in the $FA_{0.4}MA_{0.6}PbI_3$ film increases. Consequently, the dips in Fig. 3(b) depict the strongest resonance thickness conditions for the active layer. Additionally, dips in Fig. 3(b) indicates that the resonance thickness condition should be a series of discrete values, any slight deviation toward larger or smaller values of h_4 will result in a rapid decrease in resonance intensity. Related simulation results and discussion can be found in the supplementary document as Fig .S3.

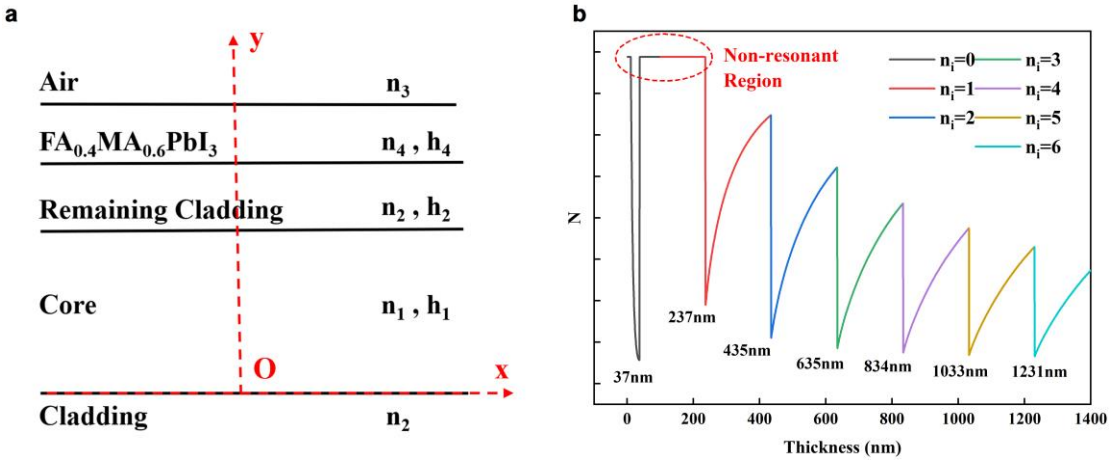

Fig. 3: Analysis of resonance thickness conditions for the active layer of AFPD. (a) A simplified slab waveguide model illustrating the intensity variation of mode field along the y-axis. (b) The curve depicting the relationship between the thickness h_4 of $FA_{0.4}MA_{0.6}PbI_3$ and effective refractive index N.

The resonance thickness conditions depicted in Fig. 3 (b) are validated by the simulation results shown in Fig. 4 (with the third order validated by Fig. 2 (b) and (c)). The intensity of electric field along the y-axis for each thickness condition is shown in Fig. 4 (g) - (i), respectively. The simulation results demonstrate the presence of a strong mode field in the perovskite film layer satisfied resonance thickness condition of each order. These resonance orders, as the interference patterns shown in Fig. 4 (a) - (f) and the peaks in (g) - (l), align consistently with theoretical analysis. With the increase in resonance order, as shown in Fig. 4 (m), the calculated resonance thickness conditions show a growing deviation from the values obtained by simulation. This discrepancy may arise from the differences between the slab waveguide model and the cylindrical waveguide structure of fiber.

These resonance thickness conditions and the active layer design method offer promising approaches for enhancing the coupling efficiency between light and the active layer, consequently improving device performance. Furthermore, Fig. 4 also demonstrates the feasibility of achieving a strong mode

field even in a thinned active layer, which presenting a potential strategy for meeting the demands of thinning the active layer while maintaining efficient light coupling and absorption for faster and higher detection response[13, 14].

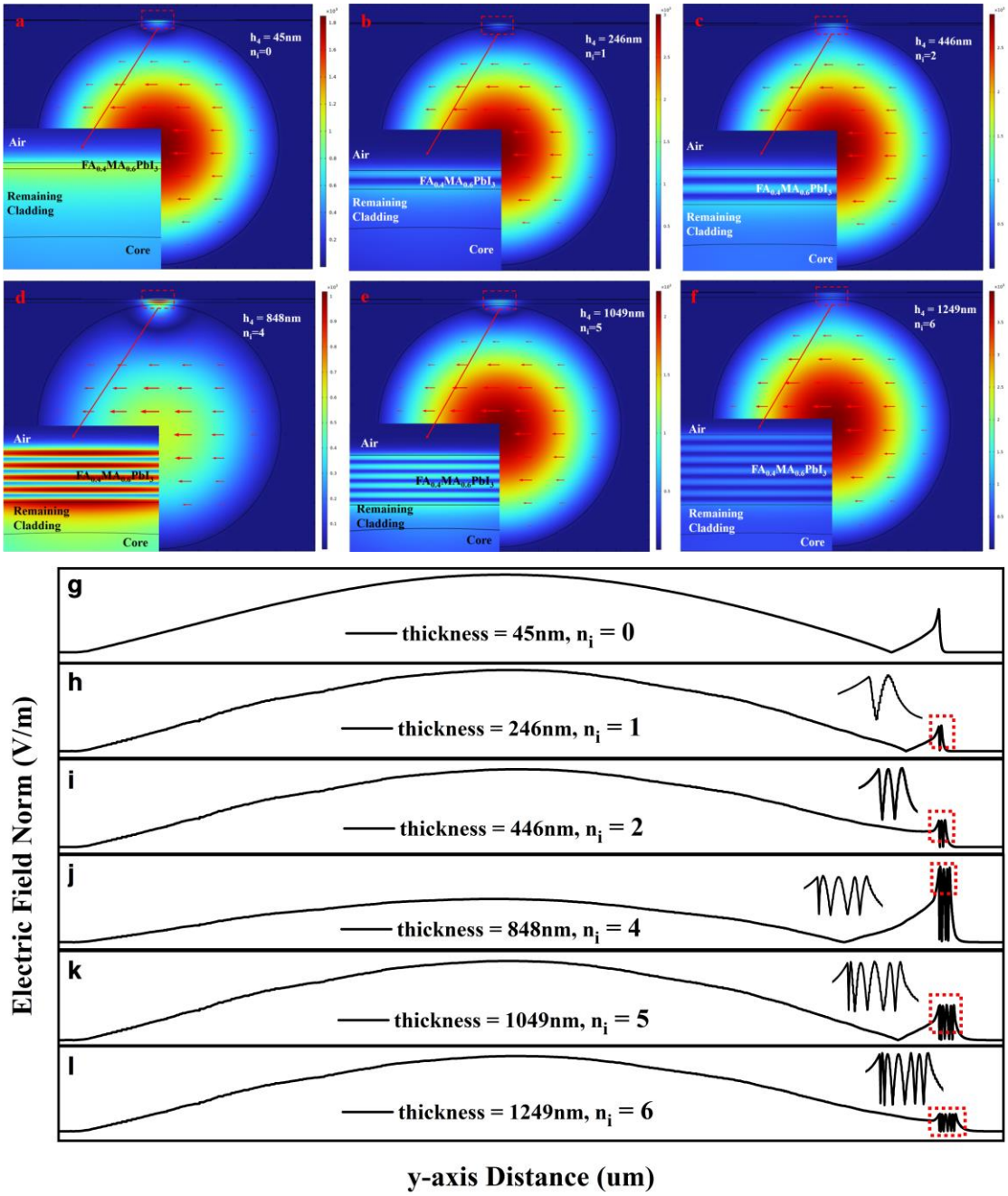

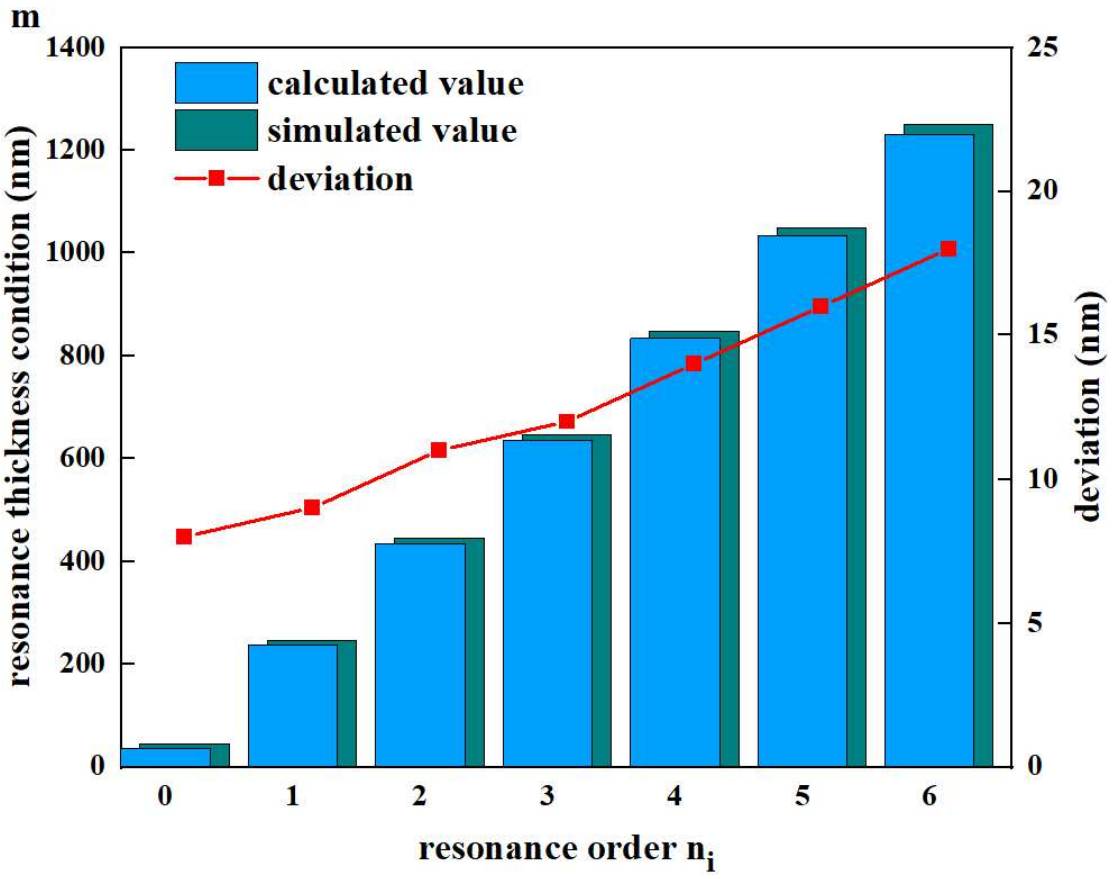

Fig. 4: Validation of the resonant thickness condition through simulation. (a) - (i) Simulation results depicting the distribution and intensity of the mode field under different resonance thickness conditions. (m) Discrepancy between simulated and calculated values.

2.3 Fabrication of AFPD

The fabrication process of the proposed AFPD is illustrated in Fig. 5. As shown in Fig. 5 (a), the SP-MMF is fixed on a glass substrate and preheated at 155°C for 10 minutes on a hot plate. The preheating process prevents the incomplete solvent evaporation during deposition and the consequent formation of yellow phase δ-$FAPbI_3$ which possess poor photoelectric performance[15]. As shown in Fig. 5 (b) and (c), perovskite thin film is deposited on the polished surface of SP-MMF at 155°C through the blade-coating method, followed by annealing at 150°C for 5 minutes. The employed precursor solution used single DMF solvent with a concentration of 40%. During the coating process, as the DMF evaporated, the perovskite crystallized into the α-phase black film, and no yellow phase δ-$FAPbI_3$ was observed. The entire deposition process is completed in air atmosphere at 24°C and 40% RH. Finally, as shown in Fig. 5(d), Ag interdigital electrodes of 100nm thick are deposited on the $FA_{0.4}MA_{0.6}PbI_3$ film by thermal evaporation. The schematic and physical images of the fabricated AFPD are shown in Fig. 5(e). The finger width and gap of the electrode mask used during the thermal evaporation process are both 40μm. The red leaked light in the Fig. 5(e) may be caused by the saturation of light absorption in the $FA_{0.4}MA_{0.6}PbI_3$ film and the roughness of the polished surface and the $FA_{0.4}MA_{0.6}PbI_3$ film surface. Microscope images of the polished surface of SP-MMF can be found in the supplementary document.

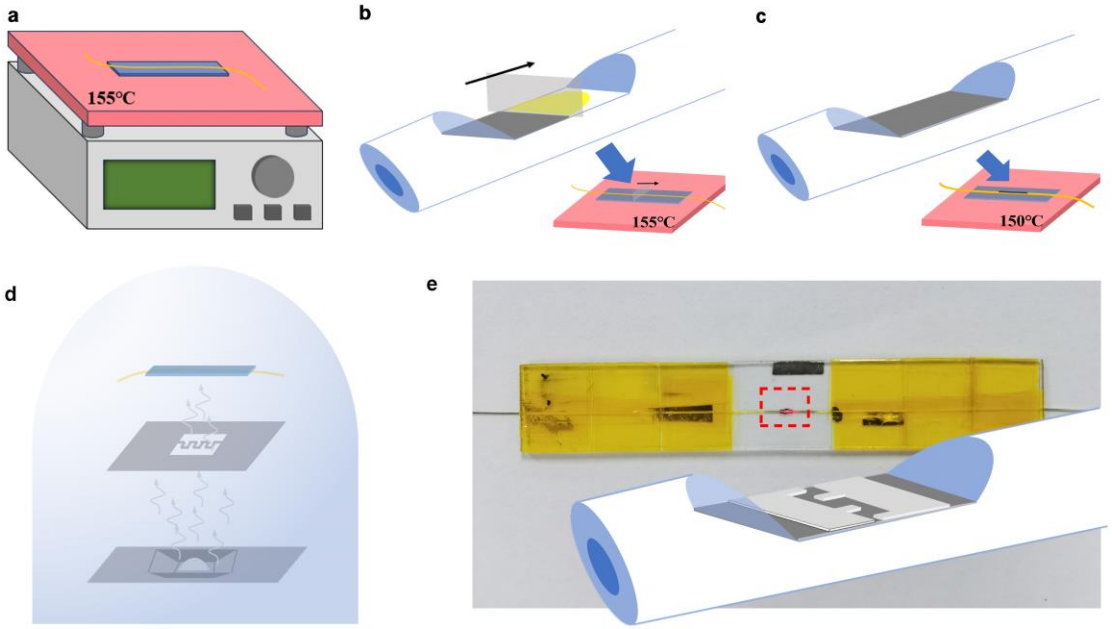

Fig. 5: Device fabrication process. (a)-(d) Schematic diagrams illustrating the device fabrication process. (e) Structural model and physical picture of the fabricated device sample.

2.4 Energy band diagram of AFPD

The band diagram of the deposited MSM photodetector is shown in Fig. 6. The work function of the $FA_{0.4}MA_{0.6}PbI_3$ film is 4.14 eV [16], and the work function of Ag film is 4.26 eV. Under ideal situation, due to the small difference between the work functions, two back-to-back shallow Schottky junctions, as depicted in Fig. 6 (a), are formed in the MSM photodetector. Under a small bias voltage, As shown in Fig. 6 (b), the photogenerated electron-hole pairs are separated by the built-in electric field and resulting in photocurrent. Under a higher bias voltage, as shown in Fig. 6 (c), the photodetection response of the device is mainly dominated by the photoconductive effect.

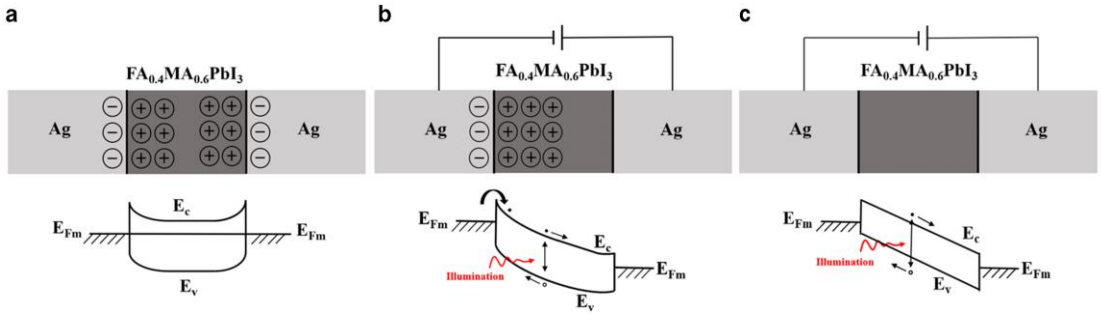

Fig. 6: Band diagrams of the MSM photodetector under equilibrium and biased conditions. (a) Band diagram of the MSM photodetector without bias voltage. (b) Band diagram of the device under a small bias voltage. (c) Band diagram under a higher bias voltage, indicating the device performs as a photoconductive detector.

2.5 Test method of AFPD

The experimental setup is depicted in Fig. 7. A 650nm laser is utilized as the light source. The 650nm light is initially transmitted by single-mode fiber (SMF), then split equally into two MMF by a 50:50 coupler. These fibers serve as the experimental and reference paths, respectively. The experimental light path is consisting of the AFPD, a semiconductor analyzer, and an optical power meter (OPM). A

portion of the transmitted light leaks through the polished surface of the SP-MMF to the active layer of the AFPD, while the remaining continues to propagate within the fiber. The semiconductor analyzer is used to obtain the I-V curve and photodetection response of the device. The OPM is utilized to measure the transmission power of the experimental light path, which is denoted as OPM_1. A MMF of the equal length to the experimental light path is utilized in reference light path to represent the intact transmitted power, which is denoted as OPM_2.

The incident power for photodetector integrated on fiber can be considered as equation (15):

$$P_{in} = OPM_1 - OPM_2 \tag{15}$$

Under a certain bias voltage, as the photocurrent for the leakage light is denoted as $I_{p\hbar}$, the dark current is denoted as I_{dark}, the responsivity R can be described as following:

$$R = \frac{I_{p\hbar} - I_{dark}}{OPM_1 - OPM_2} \tag{16}$$

The external quantum efficiency (EQE) can be obtained from the following equation:

$$EQE = R \times \frac{\hbar c}{\lambda q} \tag{17}$$

Where $\hbar$ is the Planck constant, c is the vacuum light speed, λ is the wavelength of the incident light, and q is the elementary charge.

Denoting S as the effective irradiation area, the detectivity (D^*) can be obtained from the following equation:

$$D^* = \frac{R}{\sqrt{\frac{2qI_{dark}}{S}}} \tag{18}$$

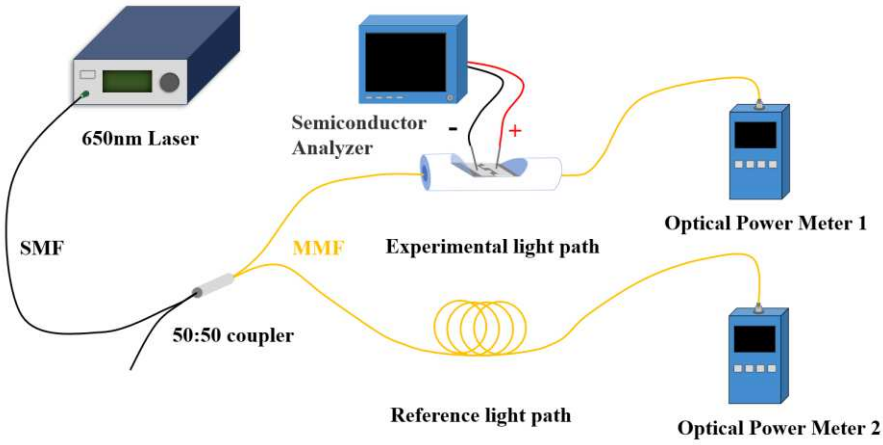

Fig. 7: Schematic of the experimental setup.

3. Results and discussion

3.1 Characterization of the fabricated films

The microscopic images of the perovskite thin film deposited on the polished surface by the blade-coating method are shown in Fig. 8 (a). The film appears black, no yellow phase δ-$FAPbI_3$ is observed. Defects of the perovskite film can be attributed to the roughness of SP-MMF's polished surface. Fig. 8 (b) displays an image of the perovskite film with Ag interdigitated electrodes. The XRD spectrum of the $FA_{0.4}MA_{0.6}PbI_3$ film prepared by blade-coating is shown in Fig. 8 (c). The characteristic peaks at 2θ = 13° and 2θ = 14.3° are corresponding to the (001) refection of PbI_2 and the (100) refection of $FA_{0.4}MA_{0.6}PbI_3$ respectively[17]. No diffraction peak of δ-$FAPbI_3$ is observed in the XRD spectrum. The intensity of the diffraction peak of $FA_{0.4}MA_{0.6}PbI_3$ is significantly higher than that of PbI_2, indicating

that most of the PbI_2 has been converted into perovskite and the film possesses high crystallinity. The UV-VIS absorption spectrum shown in Fig. 8 (d) indicates that the prepared $FA_{0.4}MA_{0.6}PbI_3$ film possesses high absorbance with an absorption edge reaching 800nm, which is close to transmission window of MMF. The images and results shown in Fig. 8 demonstrate the high quality of perovskite crystals deposited on the polished surface using blade-coating method, suggesting potential for achieving high-performance photodetector.

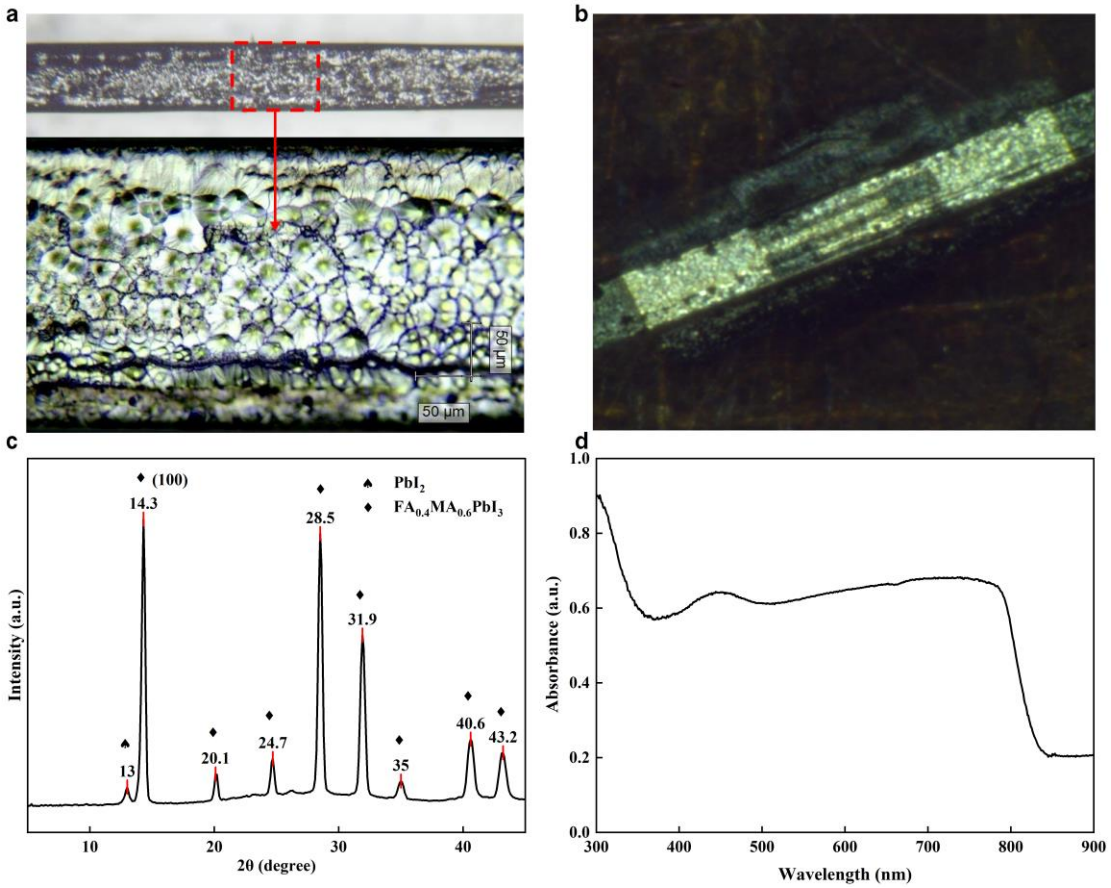

Fig. 8: Images and characterization for the deposited film. (a) Microscopic image of the $FA_{0.4}MA_{0.6}PbI_3$ thin film deposited on the polished surface of SP-MMF. (b) Microscopic image of the deposited perovskite film with Ag interdigitated electrodes. (c) XRD patterns of the fabricated $FA_{0.4}MA_{0.6}PbI_3$ thin film. (d) UV-VIS absorption spectrum of the fabricated $FA_{0.4}MA_{0.6}PbI_3$ film.

3.2 Photoresponse characterizations of the AFPD

The I-V curves of the device for different power 650nm light are shown in Fig. 9 (a), while the enlarged view of the small bias voltage range is depicted in Fig. 9 (b). Due to the symmetric structure of the MSM photodetector, the I-V curves exhibit a symmetric distribution concerning the bias voltage. Within the bias range of 0~0.1V, Schottky junction is under reverse bias, the device's current remains relatively unchanged with voltage variations. As the bias exceeds 0.1V, device's current increases rapidly with voltage, indicating a breakdown of the Schottky junction, and the I-V curves aligns with photoconductive photodetector. The phenomenon where the lowest current in the device's I-V curves, corresponding to different incident powers, is not located at V=0 can be attributed to ion migration within the perovskite film[18]. For the same incident power, photocurrent of the device increases with bias voltage, primarily due to the enhanced ability of photoconductor to separate photogenerated electron-hole pairs under higher applied bias. Furthermore, as the migration speed of photogenerated

electron rises with bias voltage, its transit time is much shorter than photogenerated holes. When photogenerated electrons are rapidly swept out to the electrode, the excess photogenerated holes still remaining in the photodetector will attract electrons back to maintain charge neutrality, resulting in multiple crossings of photogenerated electrons through the photodetector within their lifetime, thereby enhancing the gain of the photodetector. In the experiment, the dark current is measured as 16.4nA under -3V bias. When illuminated by 48.5μW 650nm light, the photocurrent achieved 7.62μA, which is 465 times the dark current. As shown in Fig. 9 (c), the device's responsivity decreases with increasing light power but increases with higher bias voltage. The former is commonly caused by the light saturation absorption in perovskite film and the enhanced recombination resulting from increased carrier concentration. The latter is attributed to the detector's enhanced ability to separate photogenerated electron-hole pairs and the raised photoconductive gain. Consequently, the EQE and D* exhibit an increasing tendency with the rise in bias voltage, as shown in Fig. 9 (d).

In the experiment, under -3V bias, the device achieves a responsivity of 3.2 A/W to 200nW 650nm light, with EQE and D* reaching 607% and 1.63×10^{10} Jones, respectively.

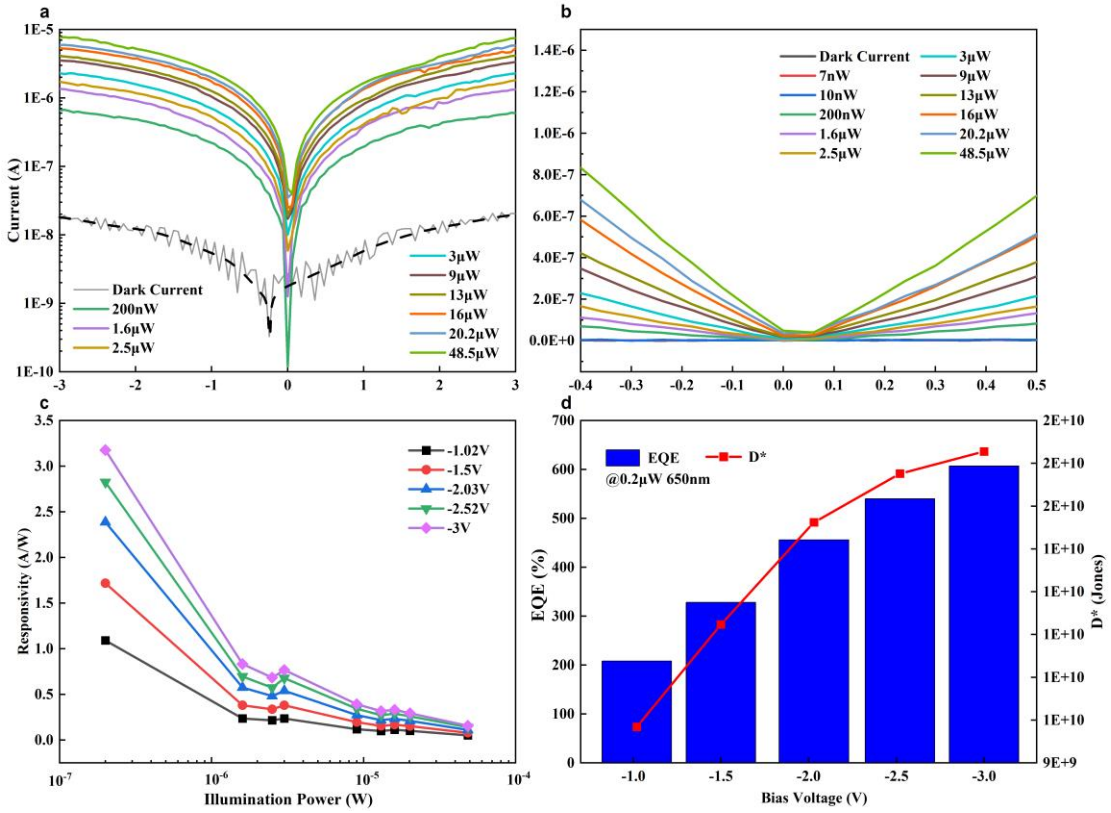

Fig. 9: AFPD response to 650nm light. (a) I-V curves of the device for different power levels of 650nm light. (b) I-V curves of low bias range where Schottky contact characteristics can be observed (c) The variation curve of the device's responsivity with increasing light power under different biases. (d) The variation trends of device's EQE and D^* with increasing bias voltage for 0.2μW 650nm light.

The result of the response time test is depicted in Fig. 10. In the experiment, pulsed light at different powers were output by 650 nm laser and utilized as the transmitted light in the fiber. The device's response time to light pulses of different powers under bias voltages of -1V, -2V, and -3V is illustrated in Fig. 10 (a), (b), and (c), respectively. When the pulsed light leaks through the polished surface of the SP-MMF to the detector, photogenerated carriers will be excited and swept out to the electrodes under the influence of the applied bias, resulting in photocurrent. In the experiment, the shortest rise time (τ_{on})

of the device achieved 8ms, and the shortest fall time (τ_{off}) achieved 3ms. For different biases, the device exhibits the shortest response time to 2.5μW 650nm light. As shown in Fig. 10 (d), the shortest overall response time was obtained under -1V bias, with both τ_{on} and τ_{off} reaching 8ms.

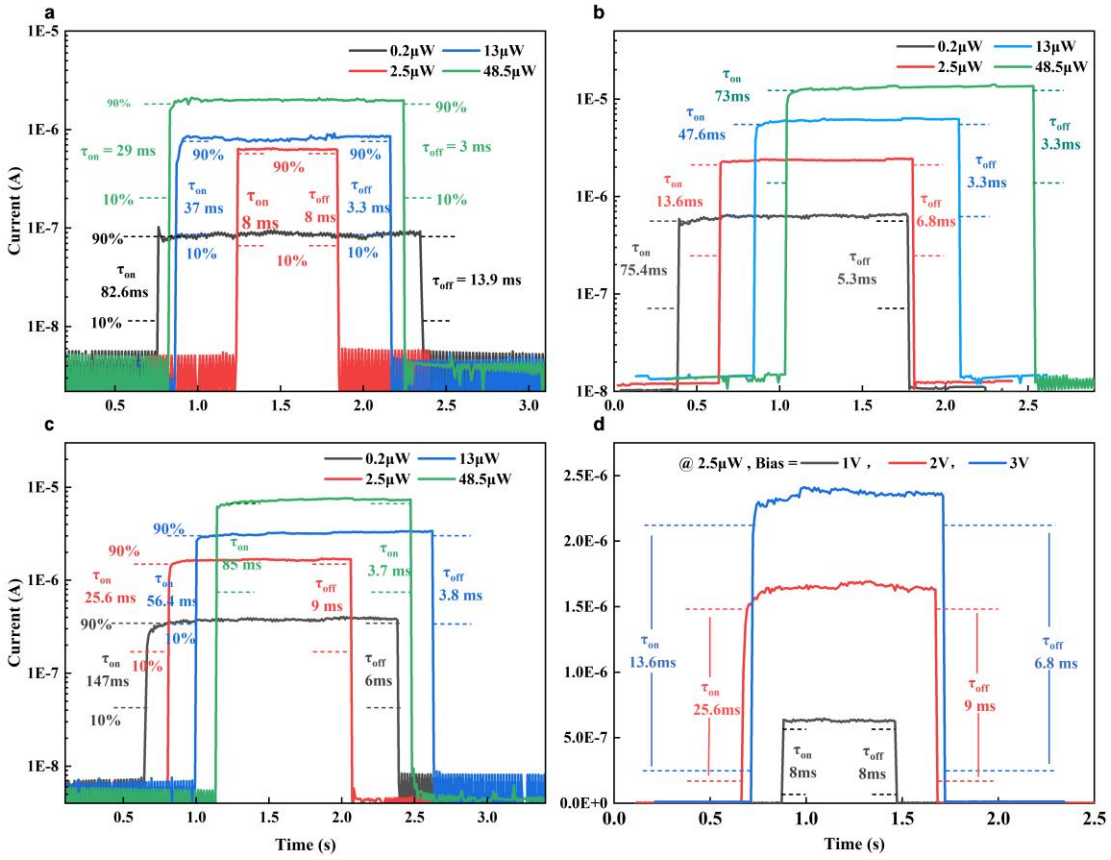

Fig. 10: Response time of the device to 650nm light under different bias voltages. (a), (b), (c) Device's response time to 650nm light of different power under bias voltages of -1V, -2V, and -3V, respectively. (d) Response time of the device to 2.5μW 650nm light under different bias voltages.

3.3 Performance comparison to similar devices

The performance comparison between the proposed AFPD and other similar photodetectors is presented in Table 1. In comparison to alternative methods, AFPD proposed in this work achieves a larger responsivity while exhibiting a shorter response time. This heightened responsivity can be attributed to the long-range effect of the fiber-integrated device form, which enhances light absorption and response by extending the material's light absorption distance.

Table 1 The performance comparison between the proposed AFPD and other similar photodetectors

Ref.	PD Structure	Materials	Responsivity	Response Time
[12]	MSM	$FA_{0.4}MA_{0.6}PbI_3$	< 1 A/W @650nm	τ_{on} = 9ms τ_{off} = 8.5ms
[19]	MSM	$MAPbI_3$ Nanowires	0.56 A/W @473nm	τ_{on} = 0.2ms τ_{off} = 0.37ms
[20]	Fiber-integrated Hybrid MSM structure	$CsPbBr_3$ /Graphene	2×10^4 A/W @400nm	τ_{on} = 3.1s τ_{off} = 24.2s
[6]	Fiber-integrated Heterostructures	Graphene /MoS_2	2.2×10^5 A/W @1550nm	τ_{on} = 57.3ms τ_{off} = 61.9ms
[10]	Fiber-integrated MSM	Graphene	1×10^4 A/W @1550nm	τ_{on} = 125ms τ_{off} = 145ms
[21]	MSM	$CsPbBr_3$/ ZnO	630 μA/W	τ_{on} = 61μs τ_{off} = 1.4ms
This study	Fiber-integrated MSM	$FA_{0.4}MA_{0.6}PbI_3$	3.2 A/W @650nm	τ_{on} = 8ms τ_{off} = 8ms

4. Conclusion

In summary, a waveguide-coupled AFPD based on $FA_{0.4}MA_{0.6}PbI_3$ perovskite has been proposed. The method of optimizing its performance by designing the thickness of the active layer is also explored based on thin-film waveguide theory. Theoretical analysis and simulation results confirm the presence of a strong mode field in the $FA_{0.4}MA_{0.6}PbI_3$ film satisfied the resonance thickness condition, which is potential to improve both the responsivity and response time of AFPD. Experiment results demonstrate that the device achieved a responsivity of 3.2 A/W to 650 nm light with rise and fall time of 8ms each. The proposed AFPD offers a promising design for high-performance all-fiber-integrated perovskite photodetectors. Further performance improvement can be achieved by optimizing the quality of the perovskite film and precisely controlling film thickness to satisfy the resonance condition.

Data availability

The authors declare that the main data supporting the findings of this study are available within the article and its Supplementary Information file. All other relevant data supporting the findings of this study are available from the corresponding author on request.

References

1. Ahmadi M, Wu T, Hu B. A Review on Organic-Inorganic Halide Perovskite Photodetectors: Device Engineering and Fundamental Physics. *Adv Mater* **29**, 24 (2017).
2. Miao JL, Zhang FJ. Recent progress on highly sensitive perovskite photodetectors. *J Mater Chem C* **7**, 1741-1791 (2019).
3. Monroy E, Omnès F, Calle F. Wide-bandgap semiconductor ultraviolet photodetectors. *Semicond Sci Technol* **18**, R33-R51 (2003).
4. Wu D*, et al.* Universal Strategy for Improving Perovskite Photodiode Performance: Interfacial Built-In Electric Field Manipulated by Unintentional Doping. *Adv Sci* **8**, 13 (2021).
5. Huang GY*, et al.* Recent progress in waveguide-integrated photodetectors based on 2D materials for infrared detection. *J Phys D-Appl Phys* **56**, 23 (2023).
6. Zhuo LQ*, et al.* High performance multifunction-in-one optoelectronic device by integrating graphene/MoS2 heterostructures on side-polished fiber. *Nanophotonics* **11**, 1137-1147 (2022).
7. Sun XW*, et al.* Broadband photodetection in a microfibergraphene device. *Opt Express* **23**, 25209-25216 (2015).
8. Lee EJ*, et al.* Active control of all-fibre graphene devices with electrical gating. *Nat Commun* **6**, 6 (2015).
9. Zhuo LQ*, et al.* A broadband all-fiber integrated graphene photodetector with CNT-enhanced responsivity. *Nanoscale* **12**, 14188-14193 (2020).
10. Zhu WG*, et al.* Gold Enhanced Graphene-Based Photodetector on Optical Fiber with Ultrasensitivity over Near-Infrared Bands. *Nanomaterials* **12**, 14 (2022).
11. Yang YF, Luo JD, Wei AX, Liu J, Zhao Y, Xiao ZM. Study of perovskite solar cells based on mixed-organic-cation FAxMA1-xPbI3 absorption layer. *Phys Chem Chem Phys* **21**, 11822-11828 (2019).
12. Li SG*, et al.* Fast-response and high-responsivity FAxMA(1-x)PbI3 photodetectors fabricated via doctor-blading deposition in ambient condition. *Org Electron* **52**, 190-194 (2018).
13. Wang X*, et al.* Optimizing the performance of a β-Ga2O3 solar-blind UV photodetector by compromising between photoabsorption and electric field distribution. *Opt Mater Express* **8**,

2918-2927 (2018).
14. Honkanen K, Hakkarainen N, Määttä K, Kilpelä A, Kuivalainen P. High-speed metal-semiconductor-metal photodetectors fabricated on SOI-substrates. *Phys Scr* **T79**, 127-130 (1999).
15. Wang X*, et al.* Low-Temperature Aging Provides 22% Efficient Bromine-Free and Passivation Layer-Free Planar Perovskite Solar Cells. *Nano-Micro Lett* **12**, 14 (2020).
16. Li L*, et al.* Interfacial electronic structures of MoOx/mixed perovskite photodetector. *Org Electron* **65**, 162-169 (2019).
17. Luo JD, Wei AX, Luo NQ, Liu J, Zhao Y, Xiao ZM. Effect of FA+ Fraction and Dipping Time on Performance of FAxMA1-xPbI3 Films and Perovskite Solar Cells. *J Electron Mater* **49**, 7054-7064 (2020).
18. Kwon KC*, et al.* Inhibition of Ion Migration for Reliable Operation of Organolead Halide Perovskite-Based Metal/Semiconductor/Metal Broadband Photodetectors. *Adv Funct Mater* **26**, 4213-4222 (2016).
19. Wu DJ*, et al.* Welding Perovskite Nanowires for Stable, Sensitive, Flexible Photodetectors. *ACS Nano* **14**, 2777-2787 (2020).
20. Chen JH, Jing Q, Xu F, Lu ZD, Lu YQ. High-sensitivity optical-fiber-compatible photodetector with an integrated CsPbBr 3–graphene hybrid structure. *Optica* **4**, 835-838 (2017).
21. Su LX, Li TF, Zhu Y. A vertical CsPbBr3/ZnO heterojunction for photo-sensing lights from UV to green band. *Opt Express* **30**, 23330-23340 (2022).

Acknowledgments:

This work is supported by the National Natural Science Foundation of China under Grant 11874281; the Key Research and Development Program of Hebei Province of China under Grant 22371701D; the Open Project Program, Key Laboratory of Intelligent Detection and Equipment for Underground Space of Beijing-Tianjin-Hebei Urban Agglomeration, Ministry of Natural Resources under Grant ZB2022004; and the Tianjin Research Innovation Project for Postgraduate Students under Grant No. 2022SKYZ146.

Author contributions

Y.C.Z conceived the idea, prepared the sample, completed the test, analyzed the data. J.L helped in preparing the sample and testing. C.H.M helped in testing. Y.Q.F helped in preparing the sample. Y.P.M. supervised and funded the project, and also raised revision suggestions as corresponding author. X.L.L. supervised the project and helped in preparing the sample.

Competing interests

The authors declare no competing interests.

Supplementary Files

This is a list of supplementary files associated with this preprint. Click to download.

- SupplementaryInformation.docx